Microwave spectroscopy of spinful Andreev bound states in ballistic semiconductor Josephson junctions

David J. van Woerkom,[1,2] Alex Proutski,[1,2] Bernard van Heck,[3] Daniël Bouman,[1,2] Jukka I. Väyrynen,[3] Leonid I. Glazman,[3] Peter Krogstrup,[4] Jesper Nygård,[4] Leo P. Kouwenhoven,[1,2] and Attila Geresdi[1,2]

[1] *QuTech, Delft University of Technology, 2600 GA Delft, The Netherlands*
[2] *Kavli Institute of Nanoscience, Delft University of Technology, 2600 GA Delft, The Netherlands*
[3] *Department of Physics, Yale University, New Haven, CT 06520, USA*
[4] *Center for Quantum Devices and Station Q Copenhagen, Niels Bohr Institute, University of Copenhagen, Universitetsparken 5, 2100 Copenhagen, Denmark*

arXiv:1609.00333v1 [cond-mat.mes-hall] 1 Sep 2016

The superconducting proximity effect in semiconductor nanowires [1] has recently enabled the study of novel superconducting architectures, such as gate-tunable superconducting qubits [2, 3] and multiterminal Josephson junctions [4, 5]. As opposed to their metallic counterparts, the electron density in semiconductor nanosystems is tunable by external electrostatic gates providing a highly scalable and *in-situ* variation of the device properties [1–3]. In addition, semiconductors with large g-factor and spin-orbit coupling have been shown to give rise to exotic phenomena in superconductivity, such as φ_0 Josephson junctions [6] and the emergence of Majorana bound states [7, 8]. Here, we report microwave spectroscopy measurements [9] that directly reveal the presence of Andreev bound states (ABS) in ballistic semiconductor channels. We show that the measured ABS spectra is a result of transport channels with gate-tunable, high transmission probabilities up to 0.9, which is required for gate-tunable Andreev qubits [10, 11] and beneficial for braiding schemes of Majorana states [12]. For the first time, we detect excitations of a spin-split pair of ABS [13] and observe symmetry-broken ABS [14], a direct consequence of the spin-orbit coupling in the semiconductor.

The linear conductance $G = \frac{2e^2}{h}\sum T_i$ of a nanostructure between two bulk leads [15] depends on the individual channel transmission probabilities, T_i. Embedding the same structure between two superconducting banks with a superconducting gap of Δ gives rise to Andreev bound states (ABS) [16]. If the junction length is much smaller than the superconducting coherence length, ξ, i.e. in the short junction limit, then the ABS levels depend on the phase difference ϕ between the leads [17]:

$$E_{\mathrm{ABS,i}}(\phi) = \pm\Delta\sqrt{1 - T_i \sin^2\frac{\phi}{2}}\,. \tag{1}$$

These subgap states with $|E_{\mathrm{ABS}}| \leq \Delta$ are localized in the vicinity of the nanostructure extending into the banks over the length scale of ξ. Note that Eq. (1) is only valid in the absence of magnetic field, when each energy level is doubly degenerate.

Direct microwave spectroscopy has recently demonstrated the occupation of the ABS by exciting a Cooper pair in atomic junctions [9]. Unlike quasiparticle tunneling spectroscopy, which has also been used to detect ABS [18, 19], resonant excitation by microwaves is a charge parity-conserving process [20]. This property enables coherent control of ABS which is required for novel qubit architectures [11] and makes microwave spectroscopy a promising tool to detect Majorana bound states [21] in proximitized semiconductor systems [22, 23].

We investigate ABS excitations in Josephson junctions that consist of indium arsenide (InAs) nanowires covered by epitaxial aluminium (Al) shells [24]. The junction, where the superconducting shell is removed, is 100 nm (device 1, see the red box in Fig. 1a) and 40 nm long (device 2), respectively. The nanowire is then embedded in a hybrid superconducting quantum interference device (SQUID) whose second arm is a conventional $\mathrm{Al/AlO}_x\mathrm{/Al}$ tunnel junction (in yellow box), enabling the control of the phase drop ϕ by means of the applied magnetic flux Φ through the SQUID loop. In the limit of an asymmetric SQUID, where the Josephson coupling of the nanowire is much smaller than that of the tunnel junction, the applied phase φ mostly drops over the nanowire link: $\phi \approx \varphi = 2\pi\Phi/\Phi_0$, where $\Phi_0 = h/2e$ is the superconducting flux quantum. We measure the microwave response [20] of the nanowire junction utilizing the circuit depicted in Fig. 1a, where a second $\mathrm{Al/AlO}_x\mathrm{/Al}$ tunnel junction (in green box) is capacitively coupled to the hybrid SQUID and acts as a spectrometer. Further details on the fabrication process are given in the Supplementary Material.

In this circuit, inelastic Cooper-pair tunneling (ICPT, Fig. 1d) of the spectrometer junction is enabled by the dissipative environment and results in a DC current, I_{spec} [25]:

$$I_{\mathrm{spec}} = \frac{I_{\mathrm{c,spec}}^2 \mathrm{Re}[Z(\omega)]}{2V_{\mathrm{spec}}}. \tag{2}$$

Here $I_{\mathrm{c,spec}}$ is the critical current of the spectrometer junction, V_{spec} is the applied voltage bias, and $Z(\omega)$ is the circuit impedance at frequency $\omega = 2eV_{\mathrm{spec}}/\hbar$. Since $Z(\omega)$ peaks at the resonant frequencies of the hybrid SQUID [9, 25], so does the DC current I_{spec}, allowing us

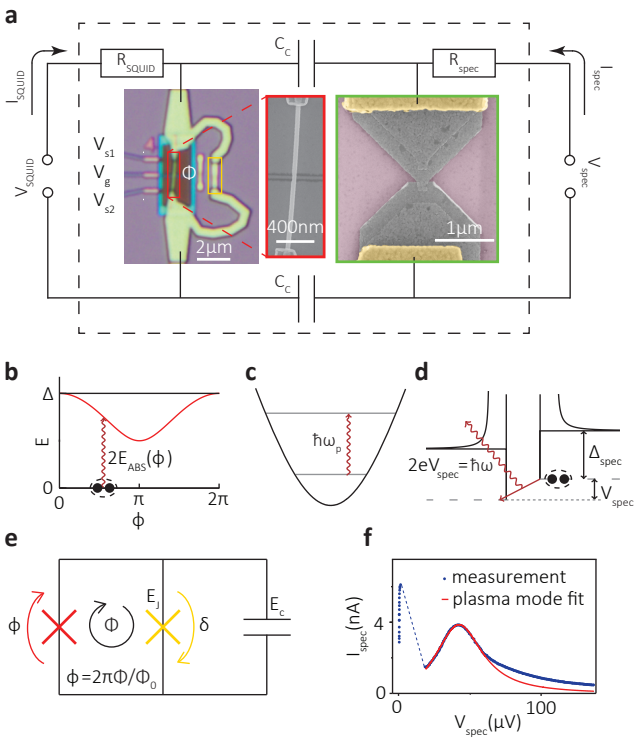

FIG. 1. **Device schematics and working principle.** (a) Equivalent circuit diagram: Bright field optical image of the hybrid SQUID with one InAs semiconductor nanowire weak link (scanning electron micrograph, in the red box) and an Al/AlO_x/Al tunnel junction (enclosed by the yellow box). The SQUID is capacitively coupled to the spectrometer Al/AlO_x/Al Josephson junction (scanning electron micrograph, in green box) via C_c. The transmission of the semiconductor channel is tuned by the gate voltage, V_g. Additional gates near the electrodes are kept at a constant voltage $V_{s1,2}$. Circuit elements within the dashed box are located on-chip, thermally anchored to 12 mK. Panels (b) and (c) show the excitations of the hybrid SQUID: the Andreev bound state at $\hbar\omega = 2E_{\rm ABS}$ (b) and the plasma oscillations at $\hbar\omega = \hbar\omega_p$ (c) are excited by a photon energy $\hbar\omega = 2eV_{\rm spec}$ set by the DC voltage bias of the spectrometer (d). (e) Schematic circuit diagram of the hybrid SQUID. The total phase $\varphi = \phi + \delta$ is determined by the applied flux Φ. (f) The measured $I(V)$ trace of the spectrometer junction with the nanowire in full depletion, i.e. in the absence of ABS excitations. The red solid line shows the fit to the circuit model of a single resonance centered at $\hbar\omega_p$, see text. Images and data were all taken on device 1.

to measure the ABS excitation energies of the nanowire junction (Fig. 1b), as well as the plasma frequency of the SQUID (Fig. 1c).

First we characterize the contribution of the plasma mode with the nanowire junction gated to full depletion, i.e. $G = 0$. We show the $I(V)$ curve of the spectrometer junction of device 1 in Fig. 1f, where we find a single peak centered at $\hbar\omega_p/2 = eV_{\rm spec} = 46\,\mu$eV and a quality factor $Q \approx 1$. In the limit of $E_C \ll E_J$, $\hbar\omega_p = \sqrt{2E_C E_J}$, where E_C is the charging energy of the circuit and E_J is the Josephson coupling of the tunnel junction (Fig. 1e). Estimating $E_J = 165\,\mu$eV from the normal state resistance [26], this measurement allows us to determine $E_C = 25.4\,\mu$eV (see the Supplementary Material). The choice of a low quality factor in combination with a characteristic impedance $Z_0 = 551\,\Omega \ll R_q = h/4e^2$ ensures the suppression of higher order transitions and parasitic resonances.

Next, we investigate the spectrometer response as a function of the gate voltage V_g applied to the nanowire. In the presence of ABS, $I_{\rm spec}$ exhibits peaks at frequencies where $\hbar\omega = 2E_{{\rm ABS},i}$ [20]. In Fig. 2a, we monitor the appearance of these peaks for an applied phase $\varphi = \pi$, where the ABS energy of Eq. (1) is $E_{{\rm ABS},i}(\pi) = \Delta\sqrt{1-T_i}$. Notably, for V_g values close to full depletion (see red bar in Fig.2a), we see a gradual decrease of $E_{\rm ABS}(\pi)$ (black dots in Fig. 2e). In this regime, we find a good correspondence with Eq. (1), assuming single channel transport, $G = \frac{2e^2}{h}T$ (red solid line in Fig. 2e). However, the observed $\Delta \approx 125\,\mu$eV is slightly smaller than the $\Delta_{\rm Al} \approx 200\,\mu$eV of the thin film Al contacts, in agreement with the presence of induced superconductivity in the nanowire [27]. Increasing V_g further, we observe a sequential appearance of peaks, which we attribute to the opening of multiple transport channels in the weak link and the consequent formation of multiple ABS [17]. We also find a strong variation of $E_{\rm ABS}$ with V_g similarly to earlier experiments [1–3], which we attribute to mesoscopic fluctuations. Note that the spectrometer response to the ABS transitions is superimposed on the plasma resonance peak. In order to achieve a better visibility of the ABS lines, we display $-d^2I_{\rm spec}/dV_{\rm spec}^2(V_{\rm spec})$ rather than $I_{\rm spec}(V_{\rm spec})$ (see Supplementary Material for comparison).

Now we turn to the flux dependence of the observed spectrum, shown in Fig. 2b and 2c for two distinct gate configurations. We find a qualitative agreement with Eq. (1) with one transport channel in Fig. 2b and several channels in Fig. 2c in addition to the plasma mode at $eV_{\rm spec} < 50\,\mu$eV confirming that the device is in the short junction limit. We also observe that the plasma mode $\hbar\omega_p$ oscillates with φ when the nanowire is gated to host open transport channels. This is expected due to the Josephson coupling of the nanowire becoming comparable to E_J, which also causes a finite phase drop, δ, over the tunnel junction (see Supplementary Material). We also note the presence of additional, weakly visible lines in the spectrum which could be attributed to higher order processes [9], although this is not confirmed by quantitative analysis.

In addition, we observe the occurrence of avoided crossings between the Andreev and plasma modes, as shown in Fig. 2d at $\varphi = \pi$. These avoided crossings require $\hbar\omega_p \approx 2\Delta\sqrt{1-T}$, which translates to a high transmission probability $T \approx 0.8 - 0.9$, and demonstrates the hybridization between the ABS excitation and the plasma

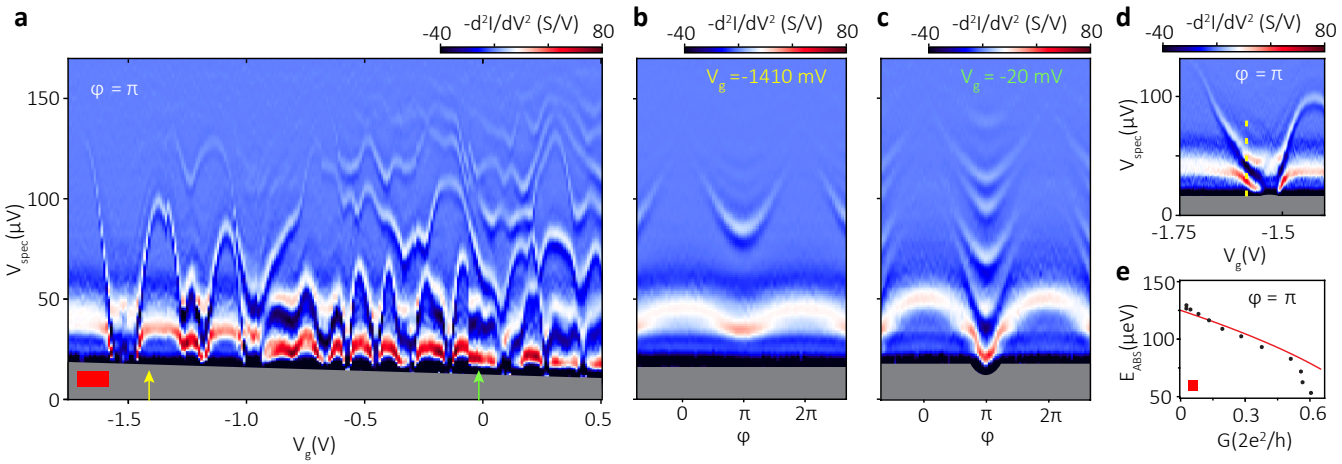

FIG. 2. **Gate dependence of Andreev bound states.** (a) $-d^2I/dV^2$ of the spectrometer junction as a function of V_g at $\varphi = \pi$, where $E_{\mathrm{ABS,i}} = \Delta\sqrt{1-T_i}$ in the short junction limit. Panels (b) and (c): $-d^2I/dV^2$ of the spectrometer junction as a function of $\varphi = 2\pi\Phi/\Phi_0$ for one channel (b) and several channels (c). The qualitative agreement of the line shapes with Eq. (1) confirms the short junction behaviour. Arrows in panel (a) indicate V_g for these measurements. Weakly visible vertically shifted replicas of the ABS lines indicate higher order transitions, see text. (d) Strong hybridization between the ABS excitation and the plasma mode with a level repulsion of $\varepsilon = 22\,\mu$eV at the yellow dash line. (e) $E_{\mathrm{ABS}}(\varphi = \pi)$ as a function of the DC linear conductance G of the nanowire weak link in the gate span denoted by the red bar in panel (a). The solid red line shows the prediction of the single channel model with $\Delta = 125\,\mu$eV, see text. All data was taken on device 1. Grey regions denote lack of data due to bias instability of the circuit.

mode. The coupling between these two degrees of freedom has previously been derived [20, 28] (see Supplementary Material), leading to an approximate formula for the energy splitting $\varepsilon \approx \Delta T\,(E_C/2E_J)^{1/4} \approx 40-70\,\mu$eV, similar to the observed value of $22\,\mu$eV.

Motivated by this observed hybridization, we provide a unified description of the energy spectrum of the circuit as a whole, and consider the following Hamiltonian for the hybrid SQUID (Fig. 1e) [10, 28, 29]:

$$\hat{H} = E_C\hat{N}^2 + E_J(1-\cos\hat{\delta}) + \hat{H}_{\mathrm{ABS}}(\varphi-\hat{\delta})\,. \qquad (3)$$

Here $\hat{\delta}$ is the operator of the phase difference across the tunnel junction, conjugate to the charge operator $\hat{N}$, $[\hat{\delta},\hat{N}] = i$. The first two terms in Eq. (3) represent the charging energy of the SQUID and the Josephson energy of the tunnel junction. The last term describes the quantum dynamics of a single-channel short weak link [10], which depends on Δ and T. For the analytic form of $\hat{H}_{\mathrm{ABS}}$, see the Supplementary Material. To fully account for the coupling between the ABS excitation and the quantum dynamics of the phase across the SQUID, we numerically solve the eigenvalue problem $\hat{H}\,\Psi = E\,\Psi$ and determine the transition frequencies $\hbar\omega = E - E_{\mathrm{GS}}$ with E_{GS} being the ground state energy.

This procedure allows us to fit the experimental data, and we find a good quantitative agreement as shown in Fig. 3a for a dataset taken at $V_g = -1410\,$mV with the fit parameters $\Delta = 122\,\mu$eV and $T = 0.57$. The previously identified circuit parameters E_J and E_C are kept fixed during the fit. We note that the observed ABS transi-

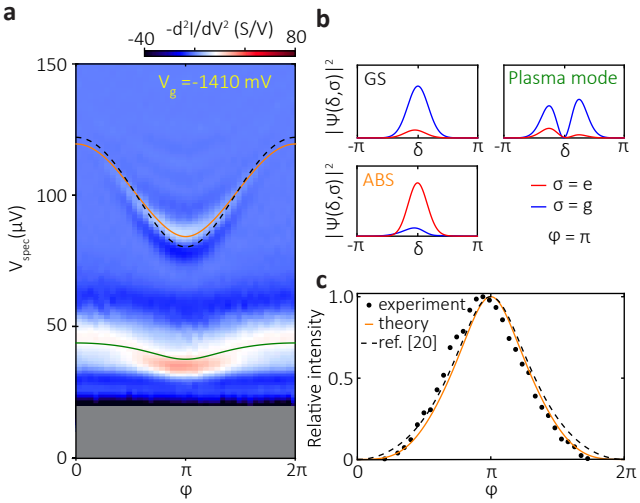

FIG. 3. **Theoretical description of the transitions.** (a) Solid lines depict the transitions identified by the model described in the text, with Δ and T being free parameters. The experimental dataset is the same as the one shown in Fig. 2b. The dashed line depicts Eq. (1) for the fitted $\Delta = 122\,\mu$eV and $T = 0.57$. (b) The probability density $|\Psi(\delta,\sigma)|^2$ in the ground state of the hybrid SQUID (GS), and in the two excited states depicted in panel (a), respectively. The weight in the ABS ground state ($\sigma = g$) and in the ABS excited state ($\sigma = e$) distinguishes between the plasma mode and the ABS. (c) The measured relative intensity of the ABS transition (black dots) compared to the theoretical expectation based on Eq. (3) (orange solid line) and from [20] (dashed black line) with no additional fitting parameters.

tion (orange solid line) only slightly deviates from Eq. (1) (black dashed line). The modulation of the plasma frequency (green solid line) is then defined by the model Hamiltonian with no additional fit parameters. We further confirm the nature of the plasma and ABS excitations by evaluating the probability density $|\Psi(\delta,\sigma)|^2$ of the eigenfunctions of Eq. (3) at $\varphi = \pi$ (Fig. 3b). In the ground state of $\hat{H}$ (GS) and in the state corresponding to the plasma excitation (green line in Fig. 3a), the probability density is much higher in the ground state of the weak link ($\sigma = g$, blue line) than in the excited state ($\sigma = e$, red line). In contrast, the next observed transition (orange line in Fig. 3a) gives rise to a higher contribution from $\sigma = e$ confirming our interpretation of the experimental data in terms of ABS excitations. Furthermore, the model can also describe measurement data with T close to 1, where it accurately accounts for the avoided crossings between the ABS and plasma spectral lines (see the Supplementary Material for a dataset with $T = 0.9$).

In Fig. 3c we show the visibility of the ABS transition as a function of the applied phase φ, which is proportional to the absorption rate of the weak link, predicted to be $\propto T^2(1-T)\sin^4(\varphi/2) \times \Delta^2/E^2_{\mathrm{ABS}}(\varphi)$ [20]. We note that in the experimental data the maximum of the intensity is slightly shifted from its expected position at $\varphi = \pi$. This minor deviation may stem from the uncertainty of the flux calibration. Nevertheless, using $T = 0.57$, obtained from the fit in Fig. 3a, we find a good agreement with no adjustable parameters (black dashed line). A similarly good correspondence is also found with the numerical model (orange line) based on Eq. (3).

We now discuss the evolution of the ABS as a function of an in-plane magnetic field B aligned parallel to the nanowire axis, which is perpendicular to the internal Rashba spin-orbit field (see the inset in Fig. 4b for measurement geometry). The applied field lifts the Kramers degeneracy of the energy spectrum, splitting each Andreev doublet into a pair $E^{\pm}_{\mathrm{ABS}}(\phi)$. For small B, the splitting $E^{+}_{\mathrm{ABS}}(\phi) - E^{-}_{\mathrm{ABS}}(\phi)$ is linear in B, due to the Zeeman effect. However, the spin-split single particle levels are not accessible by microwave spectroscopy, which can only induce transitions to a final state with two excited quasiparticles. Thus we can only measure $E_{\mathrm{tot}}(\phi) = E^{+}_{\mathrm{ABS}}(\phi) + E^{-}_{\mathrm{ABS}}(\phi)$ and expect no split of the measured spectral lines. The experimental data (Fig. 4a) shows that E_{tot} decreases with B, while the lineshape remains qualitatively intact.

In order to explain the field dependence of E_{tot}, we study the behaviour of ABS in a simple model consisting of a short Josephson junction in a one-dimensional quantum wire with proximity-induced superconductivity, Rashba spin-orbit and an applied Zeeman field parallel to the wire [22, 23]. Within this model, we are able to find E^{+}_{ABS} and E^{-}_{ABS}, and reproduce the observed quadratic decrease of the measured $E_{\mathrm{tot}}(\pi)$ (black dots in Fig. 4b).

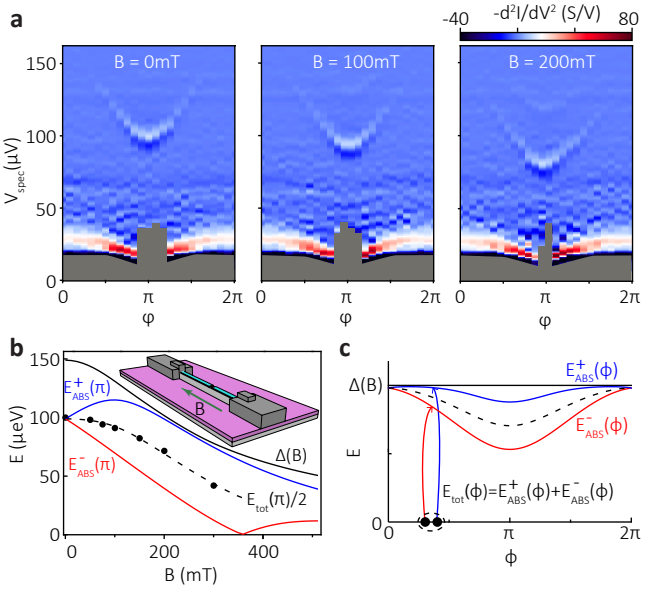

FIG. 4. **Spectroscopy of spin-split Andreev bound states in a Rashba nanowire.** Panel (a) shows the flux dependence of the Andreev bound states at $B = 0$, 100 and 200 mT, respectively, yielding to $T = 0.56$ and $\Delta = 152\,\mu$eV determined at $B = 0$. (b) Black dots depict the measured $E_{\mathrm{tot}}(\pi) = E_{\mathrm{ABS}}(\pi)^{+} + E_{\mathrm{ABS}}(\pi)^{-}$ as a function of the magnetic field B applied parallel to the nanowire, see inset. The dashed line depicts the fit to the theory with $g \approx 12$ and $\sqrt{E_{\mathrm{SO}}E_F}/\Delta \approx 0.22$, see text. The Zeeman-split ABS levels $E^{\pm}_{\mathrm{ABS}}(\pi)$ and the proximity-induced gap $\Delta(B)$ obtained from the model are shown as visual guides. (c) $E^{\pm}_{\mathrm{ABS}}(\phi)$ computed at $B = 100$ mT are shown as blue and red solid lines, together with the calculated transition energy $E_{\mathrm{tot}}(\phi)$ (black dashed line). The experimental data was taken on device 2 at $V_g = 140$ mV. Grey regions denote lack of data due to bias instability of the circuit.

Initially, as B is increased, the proximity-induced gap $\Delta(B)$ is suppressed (black solid line), while the energy $E^{+}_{\mathrm{ABS}}(\pi)$ (blue solid line) increases due to the Zeeman split of the ABS. However, a crossing of the discrete ABS level with the continuum is avoided due to the presence of spin-orbit coupling, which prevents level crossings in the energy spectrum by breaking spin-rotation symmetry. The repulsion between the ABS level and the continuum causes a downward bending of $E^{+}_{\mathrm{ABS}}(\pi)$, in turn causing a decrease in $E_{\mathrm{tot}}(\pi)$ (black dashed line).

We perform the calculations in the limit where the Fermi level E_F in the wire is well above the Zeeman energy $E_Z = \frac{1}{2}g\mu_B B$ and the spin-orbit energy $E_{\mathrm{SO}} = m\alpha^2/2\hbar^2$ with m the effective mass and α the Rashba spin-orbit coupling constant. In this case and in the short junction limit, the ratio $E_{\mathrm{tot}}(\pi)/\Delta$ is a function of just two dimensionless parameters: E_Z/Δ and $\sqrt{E_{\mathrm{SO}}E_F}/\Delta$. After extracting $\Delta = 152\,\mu$eV and $T = 0.56$ at $B = 0$ (leftmost panel in Fig. 4a), we obtain a quantitative agreement with the theory for $g \approx 12$, which is in line

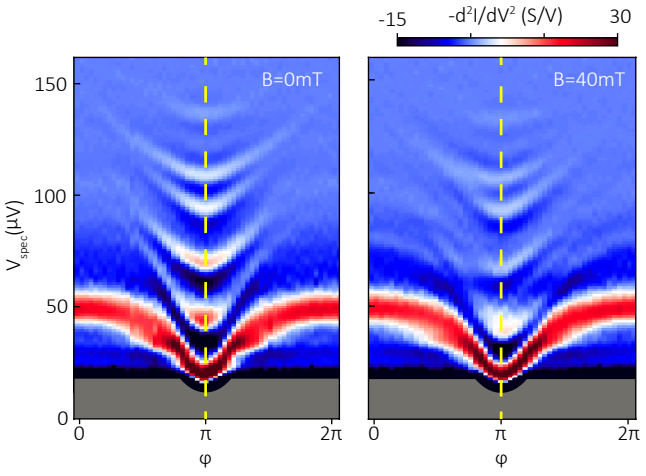

FIG. 5. **Symmetry-broken ABS in magnetic field.** The symmetry axis at $\varphi = \pi$ at zero magnetic field is denoted by dashed yellow line. Note that at $B = 40\,\mathrm{mT}$ the observed spectrum does not obey the mirror symmetry with respect to the same line. The data was taken on device 1 at $V_g = -20\,\mathrm{mV}$. Grey regions denote lack of data due to bias instability of the circuit.

with expected g-factor values in InAs nanowires [30, 31] and $\sqrt{E_{\mathrm{SO}}E_F}/\Delta \approx 0.22$. This model is consistent assuming $E_F > E_Z \approx 100\,\mu\mathrm{eV}$ at 300 mT. Thus we attain an upper bound $E_{\mathrm{SO}} \lesssim 10\,\mu\mathrm{eV}$, equivalent to a Rashba parameter $\alpha \lesssim 0.08\,\mathrm{eV\AA}$ in correspondence with earlier measurements on the same nanowires [32]. Note that E_F cannot be extracted independently from the data, thus we cannot exclude higher E_{SO} values. However, assuming the opposite regime, $E_F \approx 0$, results in a worse fit (see Supplementary Material).

Our calculations do not include the orbital effects imposed by the magnetic field on the nanowire [33] which could influence the proximity-induced superconductivity. However, the characteristic magnetic field scale is defined by $BA \approx \Phi_0$, where A is the cross-section of the nanowire. We estimate this scale to be $B \approx 300\,\mathrm{mT}$, at which field the suppression of $E_{\mathrm{tot}}(\pi)$ is already well developed. We also neglect the effect of B on the Al thin film, justified by its critical parallel field exceeding 2 T [34].

The theoretical energy spectrum shown in Fig. 4b predicts a ground state fermion-parity switch of the junction at a field $B_{\mathrm{sw}} \lesssim 400$ mT, at which the lowest ABS level $E^-_{\mathrm{tot}}(\pi) = 0$ (red line in Fig. 4b). This parity switch can inhibit the resonant excitation of the Zeeman-split ABS levels [35] thus preventing microwave spectroscopy measurements for $B > B_{\mathrm{sw}}$. This prediction is in line with the vanishing visibility of the ABS line at $B \approx B_{\mathrm{sw}}$ in the experiment.

In Fig. 5 we present data of the magnetic field dependence of the ABS excitations in the presence of several transport channels. Unlike in the single channel case (Fig. 4a), the ABS transition energies exhibit an asymmetric behavior around their minimum value at $\varphi = \pi$ in finite field (see the yellow dashed line as a guide to the eye). This behaviour is consistent with the breaking of time-reversal symmetry [36] and leads to a supercurrent $I_S(\phi) \propto \sum \partial E_{\mathrm{ABS,i}}(\phi)/\partial\phi$ which does not obey the relation $I(-\phi) = -I(\phi)$. Note however that our data does not exhibit a measurable shift of the ABS transitions, which would suggest an anomalous supercurrent $I_S(\phi = 0) \neq 0$ [14]. Rather, our measurements indicate asymmetric ABS levels when the applied magnetic field is perpendicular to the Rashba spin-orbit field with no significant shift of the energy minimum from $\phi = \pi$. Our results thus complement earlier experimental data [6] whereby a finite φ_0 shift was observed as the result of an external magnetic field applied perpendicular to the nanowire, i.e. parallel to the spin-orbit field direction. Finally, we note that the observed antisymmetric contribution changes sign for opposite magnetic field (data is presented in the Supplementary Material), as expected due to the symmetry breaking being linear in B [36].

In conclusion, we have presented microwave spectroscopy of Andreev bound states in semiconductor channels where the conductive modes are tuned by electrostatic gates and demonstrated the effect of Zeeman splitting and spin-orbit coupling. The microwave spectroscopy measurements shown here could provide a new tool for quantitative studies of Majorana bound states, complementing quasiparticle tunneling experiments. Furthermore, we have provided direct evidence for the symmetry breaking of Andreev bound states in a multichannel ballistic system. This result paves the way to novel Josephson circuits, where the critical current depends on the current direction, leading to supercurrent rectification effects [37, 38] tuned by electrostatic gates.

The authors thank L. Bretheau, Ç. Ö. Girit, L. DiCarlo, M. P. Nowak and A. R. Akhmerov for fruitful discussions, and R. van Gulik, T. Kriváchy, A. Bruno, N. de Jong, J. D. Watson, M. C. Cassidy, R. N. Schouten and T. S. Jespersen for assistance with fabrication and experiments. This work has been supported by the Danish National Research Foundation, the Villum Foundation, the Dutch Organization for Fundamental Research on Matter (FOM), the Netherlands Organization for Scientific Research (NWO) by a Veni grant, Microsoft Corporation Station Q and a Synergy Grant of the European Research Council. B. v. H. was supported by ONR Grant Q00704. L. I. G. and J. I. V. acknowledge the support by NSF Grant DMR-1603243.

Author contributions D. J. v. W., A. P. and D. B. performed the experiments. B. v. H., J. I. V. and L. I. G. developed the theory to analyze the data. P. K. and J. N. contributed to the nanowire growth. D. J. v. W., A. P. and D. B. fabricated the samples. L. P. K. and A. G. designed and supervised the experiments. D. J. v. W., B. v. H., L. P. K. and A. G. analyzed

the data. The manuscript has been prepared with contributions from all the authors.

[1] Y.-J. Doh, J. A. van Dam, A. L. Roest, E. P. A. M. Bakkers, L. P. Kouwenhoven, and S. De Franceschi, Science **309**, 272 (2005).

[2] T. W. Larsen, K. D. Petersson, F. Kuemmeth, T. S. Jespersen, P. Krogstrup, J. Nygård, and C. M. Marcus, Phys. Rev. Lett. **115**, 127001 (2015).

[3] G. de Lange, B. van Heck, A. Bruno, D. J. van Woerkom, A. Geresdi, S. R. Plissard, E. P. A. M. Bakkers, A. R. Akhmerov, and L. DiCarlo, Phys. Rev. Lett. **115**, 127002 (2015).

[4] S. R. Plissard, I. van Weperen, D. Car, M. A. Verheijen, G. W. G. Immink, J. Kammhuber, L. J. Cornelissen, D. B. Szombati, A. Geresdi, S. M. Frolov, L. P. Kouwenhoven, and E. P. A. M. Bakkers, Nat. Nano. **8**, 859 (2013).

[5] R.-P. Riwar, M. Houzet, J. S. Meyer, and Y. V. Nazarov, Nat. Comm. **7**, 11167 (2016).

[6] D. B. Szombati, S. Nadj-Perge, D. Car, S. R. Plissard, E. P. A. M. Bakkers, and L. P. Kouwenhoven, Nat. Phys. **12**, 568 (2016).

[7] V. Mourik, K. Zuo, S. M. Frolov, S. R. Plissard, E. P. A. M. Bakkers, and L. P. Kouwenhoven, Science **336**, 1003 (2012).

[8] J. Alicea, Reports on Progress in Physics **75**, 076501 (2012).

[9] L. Bretheau, Ç. Ö. Girit, H. Pothier, D. Esteve, and C. Urbina, Nature **499**, 312 (2013).

[10] A. Zazunov, V. S. Shumeiko, E. N. Bratus, J. Lantz, and G. Wendin, Phys. Rev. Lett. **90**, 087003 (2003).

[11] C. Janvier, L. Tosi, L. Bretheau, Ç. Ö. Girit, M. Stern, P. Bertet, P. Joyez, D. Vion, D. Esteve, M. F. Goffman, H. Pothier, and C. Urbina, Science **349**, 1199 (2015).

[12] D. Aasen, M. Hell, R. V. Mishmash, A. Higginbotham, J. Danon, M. Leijnse, T. S. Jespersen, J. A. Folk, C. M. Marcus, K. Flensberg, and J. Alicea, Phys. Rev. X **6**, 031016 (2016).

[13] N. M. Chtchelkatchev and Y. V. Nazarov, Phys. Rev. Lett. **90**, 226806 (2003).

[14] T. Yokoyama, M. Eto, and Y. V. Nazarov, Phys. Rev. B **89**, 195407 (2014).

[15] R. Landauer, Physics Letters A **85**, 91 (1981).

[16] I. O. Kulik, Soviet Journal of Experimental and Theoretical Physics **30**, 944 (1970).

[17] C. W. J. Beenakker, Phys. Rev. Lett. **67**, 3836 (1991).

[18] J.-D. Pillet, C. H. L. Quay, P. Morfin, C. Bena, A. L. Yeyati, and P. Joyez, Nat. Phys. **6**, 965 (2010).

[19] W. Chang, V. Manucharyan, T. S. Jespersen, J. Nygård, and C. M. Marcus, Phys. Rev. Lett. **110**, 217005 (2013).

[20] F. Kos, S. E. Nigg, and L. I. Glazman, Phys. Rev. B **87**, 174521 (2013).

[21] J. I. Väyrynen, G. Rastelli, W. Belzig, and L. I. Glazman, Phys. Rev. B **92**, 134508 (2015).

[22] R. M. Lutchyn, J. D. Sau, and S. Das Sarma, Phys. Rev. Lett. **105**, 077001 (2010).

[23] Y. Oreg, G. Refael, and F. von Oppen, Phys. Rev. Lett. **105**, 177002 (2010).

[24] P. Krogstrup, N. L. B. Ziino, W. Chang, S. M. Albrecht, M. H. Madsen, E. Johnson, J. Nygård, C. Marcus, and T. S. Jespersen, Nat. Mater. **14**, 400 (2015).

[25] T. Holst, D. Esteve, C. Urbina, and M. H. Devoret, Phys. Rev. Lett. **73**, 3455 (1994).

[26] V. Ambegaokar and A. Baratoff, Phys. Rev. Lett. **10**, 486 (1963).

[27] W. Chang, S. M. Albrecht, S. Jespersen, F. Kuemmeth, P. Krogstrup, J. Nygård, and C. M. Marcus, Nat. Nano. **10**, 232 (2015).

[28] L. Bretheau, Ç. Girit, M. Houzet, H. Pothier, D. Esteve, and C. Urbina, Phys. Rev. B **90**, 134506 (2014).

[29] A. Zazunov, V. S. Shumeiko, G. Wendin, and E. N. Bratus, Phys. Rev. B **71**, 214505 (2005).

[30] A. Das, Y. Ronen, Y. Most, Y. Oreg, M. Heiblum, and H. Shtrikman, Nat. Phys. **8**, 887 (2012).

[31] A. P. Higginbotham, S. M. Albrecht, G. Kirsanskas, W. Chang, F. Kuemmeth, P. Krogstrup, T. S. Jespersen, J. Nygård, K. Flensberg, and C. M. Marcus, Nat. Phys. **11**, 1017 (2015).

[32] S. M. Albrecht, A. P. Higginbotham, M. Madsen, F. Kuemmeth, T. S. Jespersen, J. Nygård, P. Krogstrup, and C. M. Marcus, Nature **531**, 206 (2016).

[33] B. Nijholt and A. R. Akhmerov, Phys. Rev. B **93**, 235434 (2016).

[34] R. Meservey and P. Tedrow, Journal of Applied Physics **42**, 51 (1971).

[35] J. Michelsen, V. S. Shumeiko, and G. Wendin, Phys. Rev. B **77**, 184506 (2008).

[36] J.-F. Liu and K. S. Chan, Phys. Rev. B **82**, 125305 (2010).

[37] J. E. Villegas, S. Savel'ev, F. Nori, E. M. Gonzalez, J. V. Anguita, R. García, and J. L. Vicent, Science **302**, 1188 (2003).

[38] A. A. Reynoso, G. Usaj, C. A. Balseiro, D. Feinberg, and M. Avignon, Phys. Rev. Lett. **101**, 107001 (2008)

Supplementary online material
Microwave spectroscopy of spinful Andreev bound states in ballistic semiconductor Josephson junctions

DEVICE FABRICATION

The devices are fabricated on commercially available undoped Si wafers with a 285 nm thick thermally grown SiO_x layer using positive tone electron beam lithography. First, the electrostatic gates and the lower plane of the coupling capacitors are defined and Ti/Au (5 nm/15 nm) is deposited in a high-vacuum electron-beam evaporation chamber. Next, the decoupling resistors are created using Cr/Pt (5 nm/25 nm) with a track width of 100 nm, resulting in a characteristic resistance of $100\,\Omega/\mu$m. Then, a 30 nm thick SiN_x layer is sputtered and patterned to form the insulation for the coupling capacitors and the gates. In the following step, the tunnel junctions are created using the Dolan bridge technique by depositing 9 and 11 nm thick layers of Al with an intermediate oxidization step *in-situ* at 1.4 mbar for 8 minutes. Then, the top plane of the coupling capacitors is defined and evaporated (Ti/Au, 20 nm/100 nm) after an *in-situ* Ar milling step to enable metallic contact to the Al layers. Next, the InAs nanowire is deterministically deposited with a micro-manipulator on the gate pattern. The channel is defined by wet chemical etch of the aluminium shell using Transene D at 54 °C for 12 seconds in case of device 1 and by *in-situ* patterning for device 2. Finally, the nanowire is contacted to the rest of the circuit by performing Ar plasma milling and subsequent NbTiN sputter deposition to form the loop of the hybrid SQUID. We show the design parameters of the devices in Table S1.

	Device 1	Device 2
Channel length (nm)	100	40
Tunnel junction area (nm^2)	400×120	200×120
Flux periodicity (μT)	38	120
Spectrometer junction area (nm^2)	120×120	120×120

TABLE S1. **Geometry of the devices featured in the current study.**

MEASUREMENT SETUP

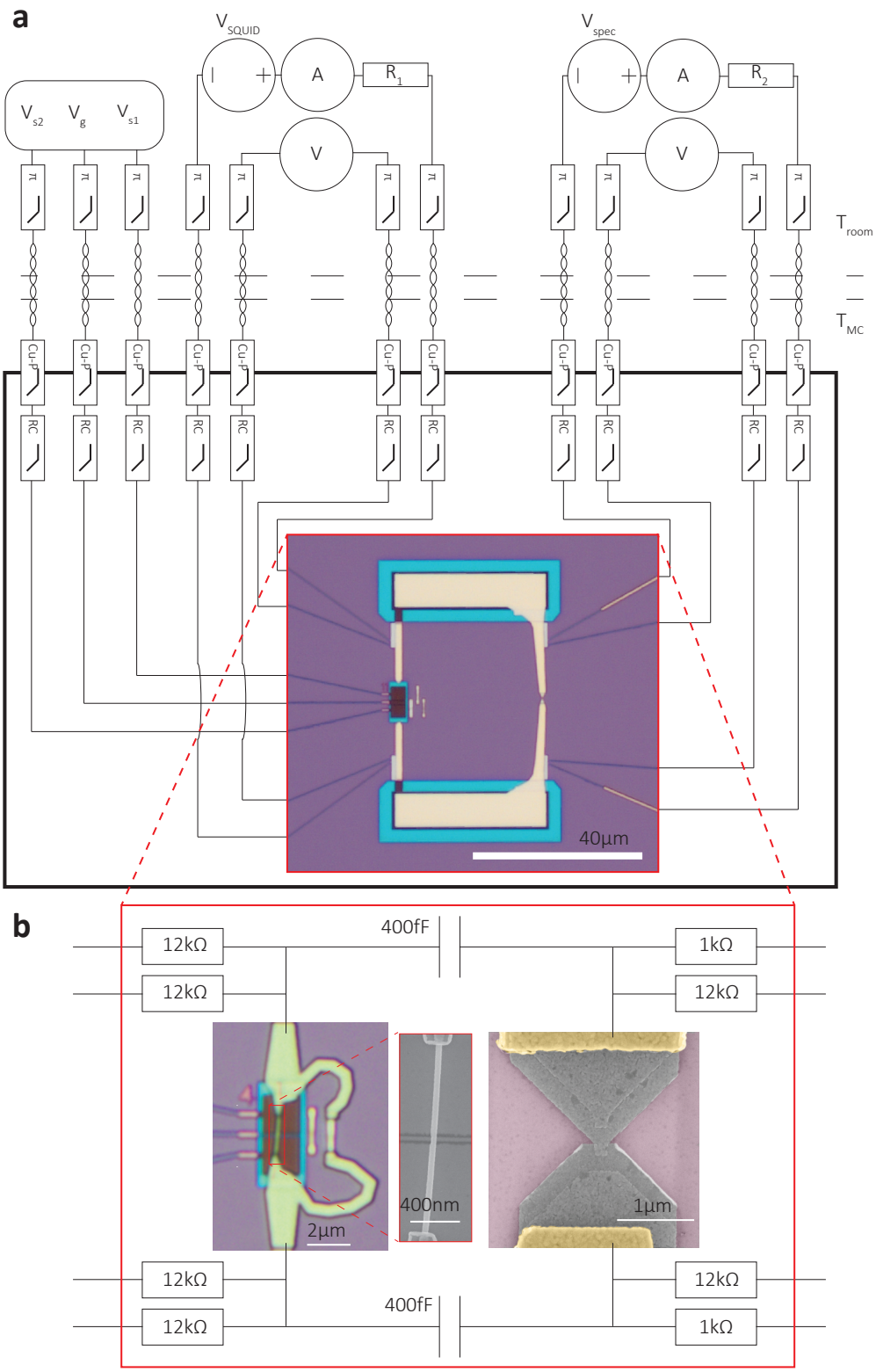

FIG. S1. **Detailed schematics of the measurement setup.** The inset of panel (a) shows a bright field optical image of device 1 before the nanowire deposition step. (b) On-chip lumped circuit elements attached to the hybrid SQUID (on the left) and the spectrometer Josephson junction (on the right).

The measurements were performed in a Leiden Cryogenics CF-1200 dry dilution refrigerator with a base temperature of 12 mK equipped with Cu/Ni shielded twisted pair cables thermally anchored at all stages of the refrigerator to facilitate thermalization. Noise filtering is performed by a set of π-LC filters ($\sim$ 100 MHz) at room temperature and copper-powder filters ($\sim$ 1 GHz) in combination with two-pole RC filters ($\sim$ 100 kHz) at base temperature for each measurement line. The schematics of the setup is shown in Fig. S1.

DEVICE CIRCUIT PARAMETERS

We characterise the circuit based on the plasma resonance observed with the semiconductor nanowire gated to zero conductance, i.e. full depletion. In this regime, we infer the environmental impedance $\mathrm{Re}[Z(\omega)]$ based on Eq. (2) in the main text and assume the following form, which is valid for a parallel LCR circuit:

$$\mathrm{Re}[Z(x)] = \frac{Z_0 Q}{1 + \frac{Q^2}{x^2}(1-x^2)^2}, \tag{S1}$$

with $x = \omega/\omega_0$ the dimensionless frequency. The resonance of the circuit is centered at $\omega_0 = (LC)^{-1/2}$ with a quality factor of $Q = R\sqrt{\frac{C}{L}}$ and a characteristic impedance of $Z_0 = \sqrt{L/C}$. Consistently with this single mode circuit, we find one peak in the $I(V)$ trace of the spectrometer that we fit to Eq. S1 (Fig. S2). We find a good quantitative agreement near the resonance peak, however the theoretical curve consistently deviates at higher voltages, i.e. higher frequencies. We attribute this discrepancy to additional losses or other resonant modes of the circuit not accounted for by Eq. (S1).

In addition, we use the superconducting gap and the linear resistance of the junctions to determine the Josephson energy E_J and the Josephson inductance L_J. With these, we infer the circuit parameters listed in Table S2.

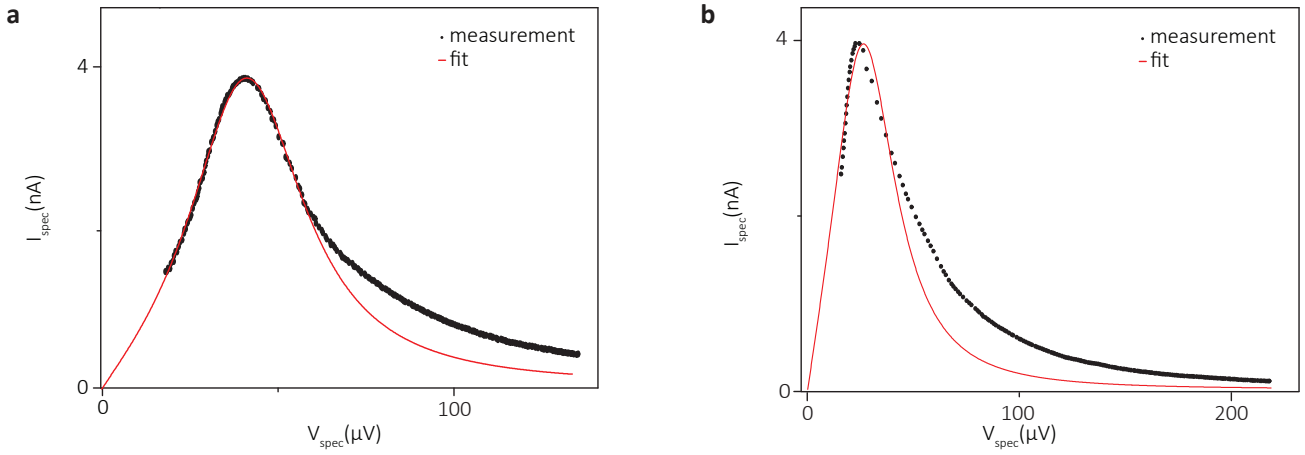

FIG. S2. **Plasma resonance of the circuit.** The measured (black dots) and fitted (solid red line) $I(V)$ trace of the spectrometer junction for device 1 (a) and for device 2 (b) respectively. The fits are based on Eq. (S1), see text. Note that we omitted the supercurrent branch for clarity.

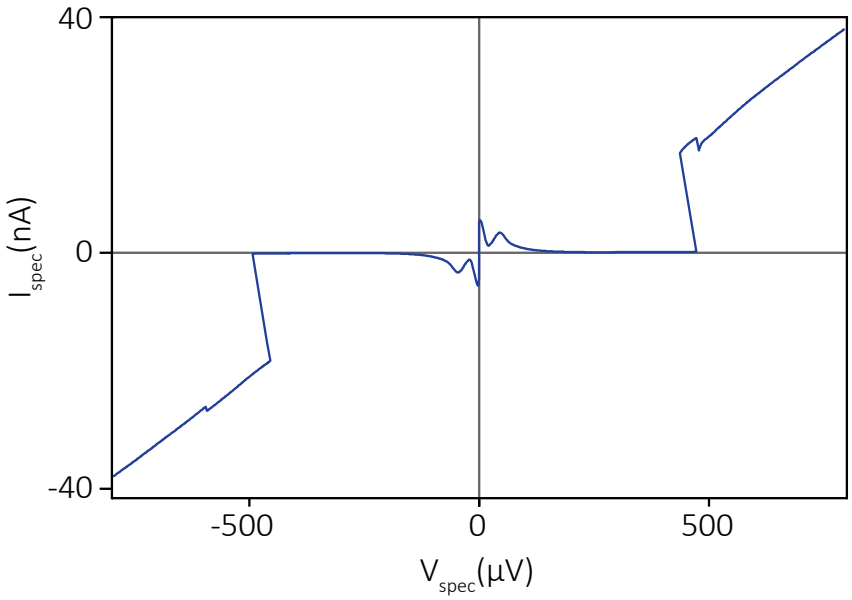

FIG. S3. **Large scale I(V) trace of the spectrometer junction.** The subgap features are shown in detail in Fig. S2a. The back-bending near $eV_{\rm spec} \approx 2\Delta_{\rm spec} = 482\,\mu$eV is attributed to a local overheating of the junction due to a large quasiparticle current density above the gap edge. The data was taken on device 1.

	Device 1	Device 2
Tunnel junction resistance R_J (kΩ)	4.80	10.7
Tunnel junction gap Δ_J (μeV)	245	250
Tunnel junction critical current $I_{\rm c,J} = \frac{\pi\Delta_J}{2eR_J}$ (nA)	80.2	36.7
$E_J = \frac{\hbar I_{\rm c,J}}{2e}$ (μeV)	165	75.5
Tunnel junction inductance $L_J = \frac{\Phi_0}{2\pi I_{\rm c,JJ}}$ (nH)	4.10	8.94
Spectrometer resistance $R_{\rm spec}$ (kΩ)	17.1	18.4
Spectrometer gap $\Delta_{\rm spec}$ (μeV)	241	249
Spectrometer critical current $I_{\rm c,spec} = \frac{\pi\Delta_{\rm spec}}{2eR_{\rm spec}}$ (nA)	22.2	21.3
Shunt resistance R (Ω)	634	743
Shunt capacitance C (fF)	12.6	11.1
Charging energy $E_c = \frac{2e^2}{C}$ (μeV)	25.44	29.1
Plasma frequency $f_p = \frac{1}{2\pi\sqrt{L_J C}}$ (GHz)	22.9	16.0
Characteristic impedance $Z_0 = \sqrt{\frac{L_J}{C}}$ (Ω)	551	897
Quality factor $Q = R\sqrt{\frac{C}{L_J}}$	1.15	0.83

TABLE S2. **Circuit parameters of the devices featured in the current study.**

ADDITIONAL DATASETS

Spectrum analysis

Peaks in the $I(V)$ trace of the spectrometer correspond to peaks in $\mathrm{Re}[Z(\omega)]$, i.e. allowed transitions of the environment coupled to the spectrometer. In order to remove the smooth background of the plasma mode (see Fig. S2), we evaluate $-d^2I/dV^2(V)$, the second derivative of the $I(V)$ to find peaks in $\mathrm{Re}[Z(\omega)]$. We benchmark this method in Fig. S4, and find that the peaks where $-d^2I/dV^2(V) > 0$ correspond to the peaks in $I(V)$ and hence $-d^2I/dV^2(V)$ is a good measure of the transitions detected by the spectrometer junction.

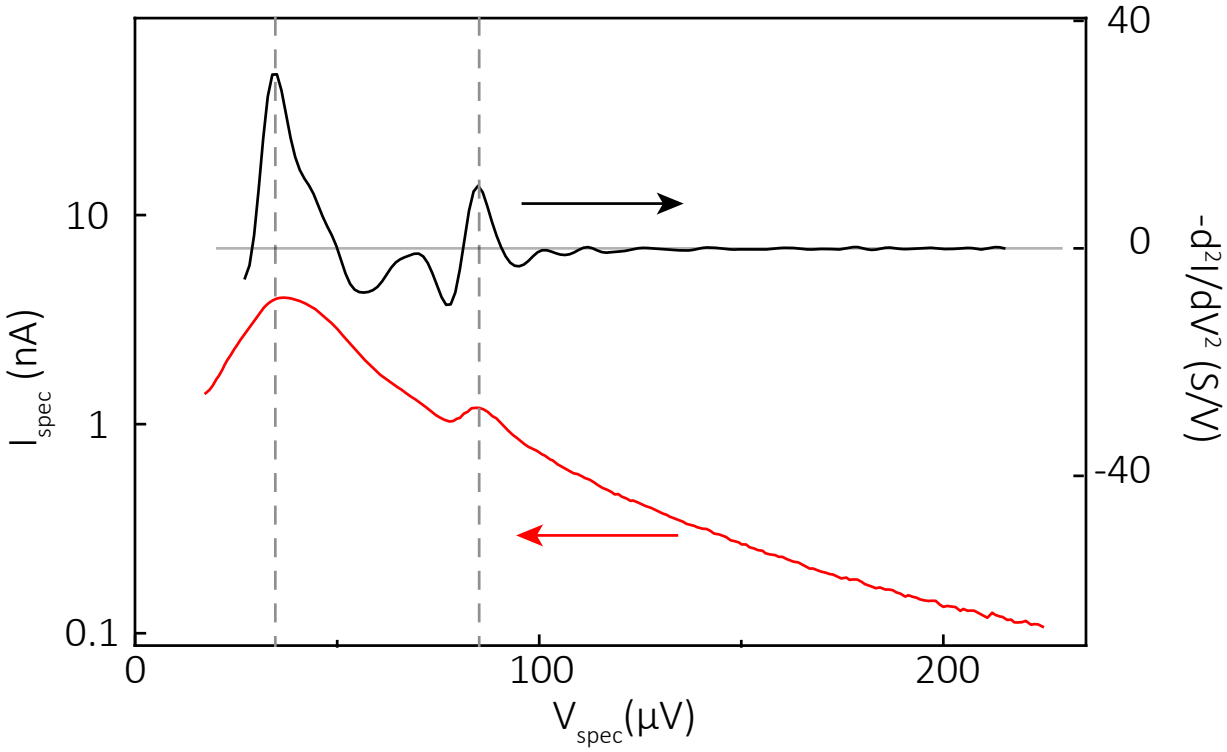

FIG. S4. **Spectrum analysis.** The $I(V)$ (red line, left axis) and the corresponding $-d^2I/dV^2(V)$ trace (black line, right axis) of the spectrometer showing the same peaks denoted by dash lines. Note that only peaks above $-d^2I/dV^2(V) = 0$ (grey horizontal line) correspond to actual transitions. This dataset was taken on device 1, at $V_g = -1410\,\mathrm{mV}$, phase biased to $\varphi = \pi$.

I(V) trace of the hybrid SQUID

We measure the $I(V)$ trace of the hybrid SQUID as a function of the gate voltage V_g at $V_{\mathrm{spec}} = 0$ (Fig. S5) and find that the subgap conductance increases with increasing gate voltage, in qualitative agreement with the contribution of multiple Andreev reflection (MAR). The zero voltage data corresponds to the supercurrent branch and the dashed lines denote the bias range where there is no data due to the bias instability of the driving circuit. In addition, we find a back-bending at the gap edge $eV_{\mathrm{SQUID}} = 2\Delta_J$, attributed to self-heating effects in the tunnel junction.

We evaluate G in Fig. 2e of the main text in the bias voltage range $V_{\mathrm{SQUID}} = 350 \ldots 430\,\mu\mathrm{V} > 2\Delta$. We note that due to the soft superconducting gap in the nanowire junction, we did not identify MAR features after subtracting the current background of the tunnel junction.

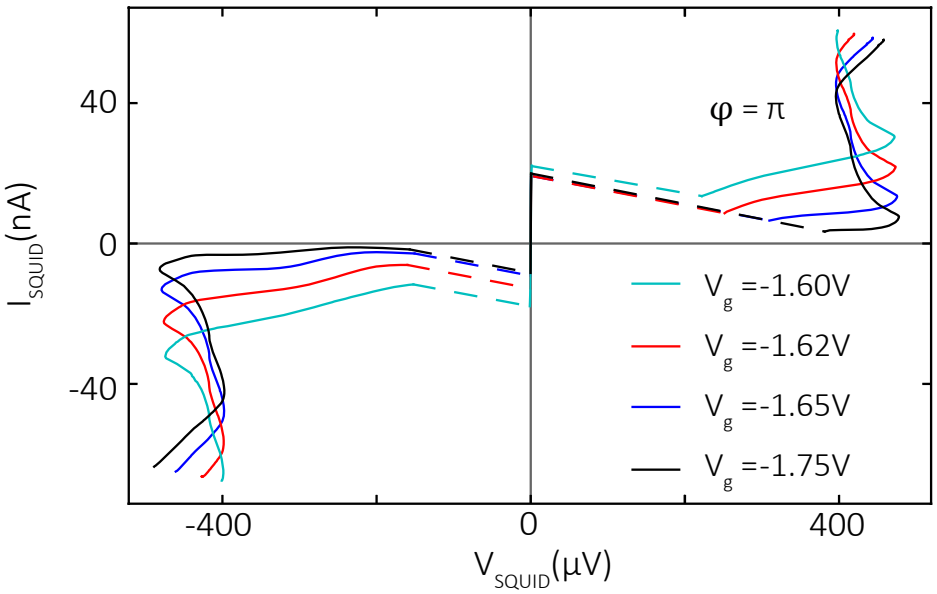

FIG. S5. **The $I(V)$ trace of the hybrid SQUID.** At $V_g = -1.75\,\mathrm{V}$, the nanowire is in full depletion, thus the corresponding $I(V)$ trace represents the Al/AlO_x/Al tunnel junction in the hybrid SQUID. The bias voltage V_{SQUID} was swept from the left to the right. The data was taken on device 1.

Fit of ABS with high transmission

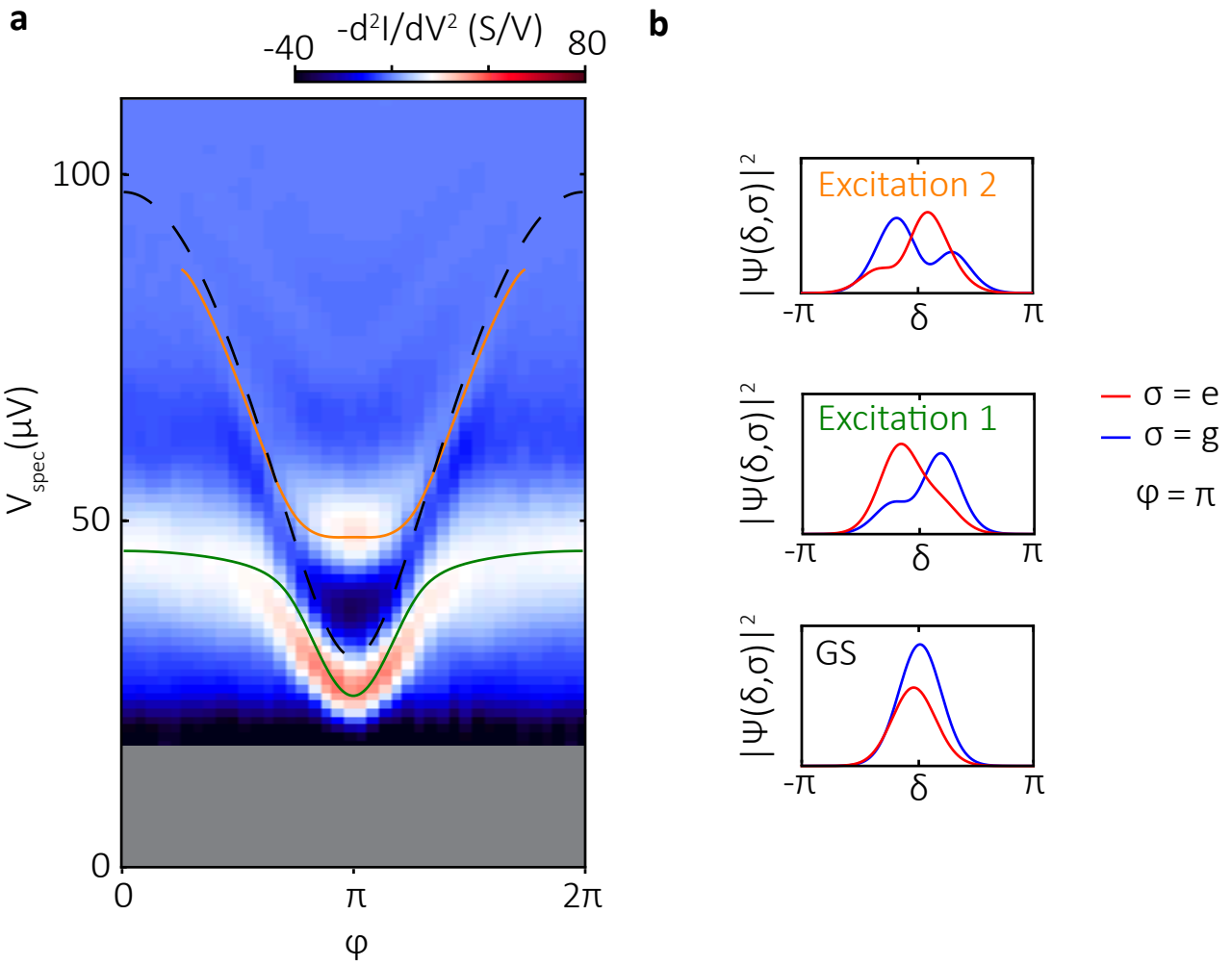

FIG. S6. **Experimental data and fit to the theory for ABS with high transmission.** In this figure we show the numerical fit to the model of Eq. (3), similarly to Fig. 3a, but for a different dataset taken at $V_g = -1.525\,\mathrm{V}$ on device 1. The figure shows that the model of Eq. (3) can accurately predict the avoided crossing originating in the coupling between the ABS and the plasma mode. Best-fit parameters are $\Delta = 97.5 \pm 1.7\,\mu\mathrm{eV}$ and $T = 0.90 \pm 0.01$. Dashed line denotes the undressed Andreev level defined by Eq. (1) in the main text. We note that the extracted value for Δ is lower than in Fig. 3a. This may be due to the fit underestimating the gap, since most of the datapoints are around $\varphi = \pi$, or due to a genuine dependence of Δ on V_g. In panel (b), we show the probability density for the ground state (GS) and the two observed excited states denoted by the green and orange lines, respectively in panel (a) at $\varphi = \pi$.

Symmetry-broken ABS in bipolar magnetic field

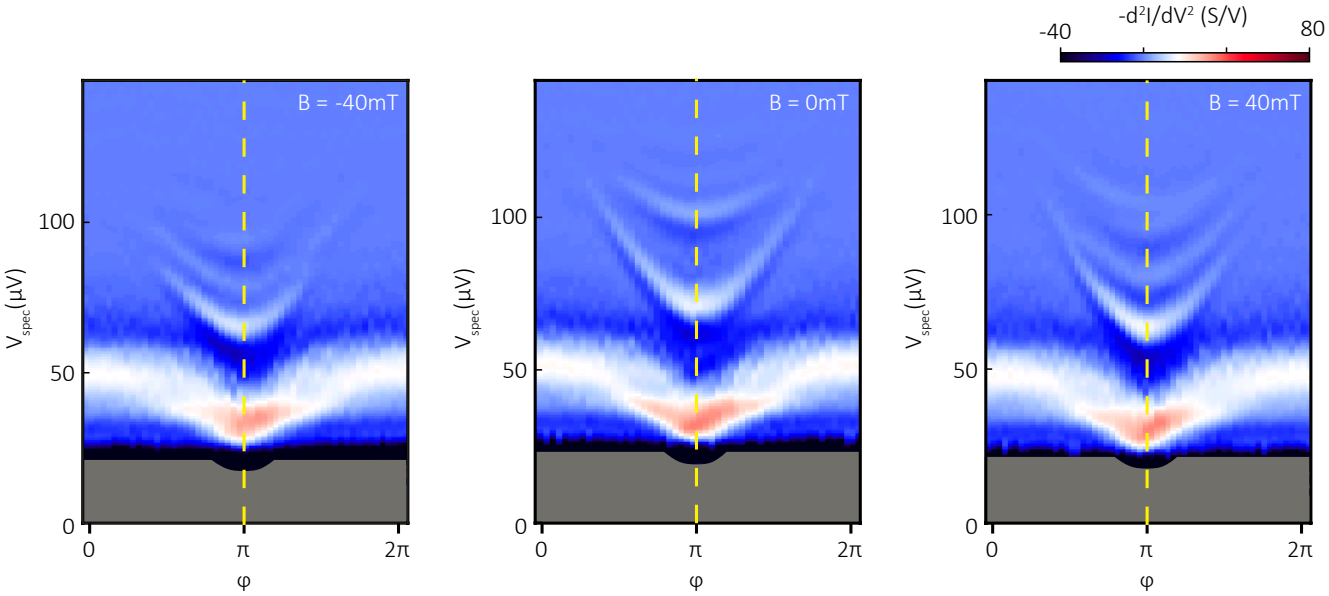

FIG. S7. **Symmetry-broken ABS in a bipolar magnetic field.** The full spectrum is symmetric around $\varphi = \pi$ at zero magnetic field (center panel) with the mirror axis denoted by the yellow dashed line. Note the asymmetry of the two lowermost ABS transitions at $B = \pm 40\,\mathrm{mT}$. The antisymmetric contribution is most visible at $V_{\mathrm{spec}} \approx 100\,\mu\mathrm{V}$, which develops an opposite shift for positive and negative magnetic fields, respectively. The data was taken on device 1 at $V_g = -770\,\mathrm{mV}$. Grey regions denote lack of data due to bias instability of the circuit.

THEORY

Estimate of the ABS-plasma resonance avoided crossing

Before describing the quantum model of the circuit in detail, we discuss the estimate for the energy splitting at the avoided crossing between the ABS transition and the plasma frequency shown in Fig. 2d.

For simplicity, we model the plasma oscillations as a bosonic mode with a flux-independent frequency given by $\hbar\omega_p = \sqrt{2E_J E_C}$, and the weak link as a two-level system, with energies $\pm E_{\rm ABS}(\varphi)$ defined by Eq. (1) in the main text. This system with the two independent degrees of freedom is described by the Hamiltonian $\hat{H}_0 = \hbar\omega_p(\hat{a}^\dagger\hat{a}+\frac{1}{2})+E_{\rm ABS}\,\hat{\sigma}_3$. Next, we add the coupling term corresponding to the excitation of the weak link due to the voltage oscillations induced by the junction in the form

$$H_g(\varphi) = g(\varphi)\,\sqrt{z}\,(\hat{a}^\dagger + \hat{a})\,\hat{\sigma}_1. \tag{S2}$$

where $z = \sqrt{E_C/2E_J}$. This term describes a linear coupling between the two-level system and the phase difference across the junction. $g(\varphi)$ is then given by the current matrix element between the ground and excited states of the weak link, which was derived in Ref. [39]:

$$g(\varphi) = \Delta\, T\sqrt{1-T}\,\sin^2(\varphi/2)\frac{\Delta}{E_{\rm ABS}(\varphi)}\,. \tag{S3}$$

The square of this current matrix element gives the microwave absorption rate of the weak link, plotted in Fig. 3c (black dashed line) of the main text. From the coupling Hamiltonian, we immediately obtain that at $\varphi = \pi$, the splitting is

$$\varepsilon = \Delta\, T\,\sqrt{z} \tag{S4}$$

which is the expression used for the estimate in the main text. We note that Eq. (S4) is the lowest-order estimate of the avoided crossing in the small parameter $\sqrt{z}$. The relatively high value $\sqrt{z} \approx 0.52$ of device 1 may explain the discrepancy between this simple estimate and the observed value which will be captured by the full model, see below. Finally, we note that the expression (S3) was also derived in Ref. [40] starting from the full model (see next section). In particular, the quantity $\Omega_x(\varphi)$ in Ref. [40] is equal to $\sqrt{z}\,g(\varphi)$.

Hamiltonian description of the hybrid SQUID

We now describe the theoretical model of the hybrid SQUID that was used to fit the experimental data. Our model is based on Refs. [41] and [42]. The Hamiltonian of the model is Eq. (3) of the main text, repeated here for convenience:

$$\hat{H} = E_C\hat{N}^2 + E_J(1-\cos\hat{\delta}) + \hat{H}_{\rm ABS}(\varphi-\hat{\delta})\,, \tag{S5}$$

with $[\hat{\delta},\hat{N}] = i$. The Hamiltonian of the weak link is [41]

$$\hat{H}_{\rm ABS}(\phi) = \Delta\,\hat{U}(\phi)\,\left[\cos(\phi/2)\,\hat{\sigma}_3 + \sqrt{1-T}\,\sin(\phi/2)\,\hat{\sigma}_2\right]\,\hat{U}^\dagger(\phi)\,, \tag{S6}$$

with $\hat{U}(\phi) = \exp\left(-i\,\sqrt{1-T}\,\hat{\sigma}_1\,\phi/4\right)$. Here $\hat{\sigma}_2$ and $\hat{\sigma}_3$ are two Pauli matrices which act on a space formed by the ground state of the weak link and an excited state with a pair of quasiparticles in the weak link. By expanding the product above, the Hamiltonian can be put in the form $\hat{H}_{\rm ABS}(\phi) = V_2(\phi)\,\hat{\sigma}_2 + V_3(\phi)\,\hat{\sigma}_3$. The two functions V_2 and V_3 are:

$$V_2(\phi) = \Delta\,\sqrt{1-T}\sin\left(\phi/2\right)\cos\left(\sqrt{1-T}\phi/2\right) - \Delta\,\cos\left(\phi/2\right)\sin\left(\sqrt{1-T}\phi/2\right)\,, \tag{S7}$$

$$V_3(\phi) = \Delta\,\sqrt{1-T}\sin\left(\phi/2\right)\sin\left(\sqrt{1-T}\phi/2\right) + \Delta\,\cos\left(\phi/2\right)\cos\left(\sqrt{1-T}\phi/2\right)\,, \tag{S8}$$

We introduce the ground ($|g\rangle$) and excited states ($|e\rangle$) of the weak link in the presence of an equilibrium phase difference,

$$\hat{H}_{\rm ABS}(\phi)\,|g\rangle = -E_{\rm ABS}(\phi)|g\rangle\,, \tag{S9a}$$

$$\hat{H}_{\rm ABS}(\phi)\,|e\rangle = +E_{\rm ABS}(\phi)|e\rangle\,, \tag{S9b}$$

where $E_{\rm ABS}(\phi)$ is given in Eq. (1) of the main text. In the basis $|\pm\rangle$ of eigenstates of $\hat{\sigma}_3$, $\hat{\sigma}_3|\pm\rangle = \pm|\pm\rangle$, they are given by

$$|g\rangle = c_{g+}(\phi)\,|+\rangle + c_{g-}(\phi)\,|-\rangle\,, \tag{S10a}$$
$$|e\rangle = c_{e+}(\phi)\,|+\rangle + c_{e-}(\phi)\,|-\rangle\,, \tag{S10b}$$

with coefficients

$$c_{g+}(\phi) = i\,\frac{E_A(\phi) - V_3(\phi)}{\sqrt{2E_A(\phi)[E_A(\phi) - V_3(\phi)]}}\,, \qquad c_{g-}(\phi) = \frac{V_2(\phi)}{\sqrt{2E_A(\phi)[E_A(\phi) - V_3(\phi)]}}\,, \tag{S11a}$$
$$c_{e+}(\phi) = -i\,\frac{E_A(\phi) + V_3(\phi)}{\sqrt{2E_A(\phi)[E_A(\phi) - V_3(\phi)]}}\,, \qquad c_{e-}(\phi) = \frac{V_2(\phi)}{\sqrt{2E_A(\phi)[E_A(\phi) + V_3(\phi)]}}\,. \tag{S11b}$$

The coefficients are normalized:

$$|c_{g+}(\phi)|^2 + |c_{g-}(\phi)|^2 = |c_{e+}(\phi)|^2 + |c_{e-}(\phi)|^2 = 1\,. \tag{S12}$$

To find the resonant frequencies of the hybrid SQUID, we solve the eigenvalue problem $\hat{H}|\Psi\rangle = E|\Psi\rangle$ numerically. We adopt the basis $|\delta,\pm\rangle \equiv |\delta\rangle\otimes|\pm\rangle$ for the joint eigenstates of the $\hat{\delta}$ and $\hat{\sigma}_3$ operators: $\hat{\delta}\,\hat{\sigma}_3\,|\delta,\pm\rangle = (\hat{\delta}\,|\delta\rangle)\otimes(\hat{\sigma}_3\,|\pm\rangle) = \pm\,\delta\,|\delta,\pm\rangle$. For the numerical solution, we use a truncated Hilbert space where the phase interval $[-\pi,\pi)$ is restricted to M discrete points, with lattice spacing $2\pi/M$. A complete basis of the truncated Hilbert space is given by the $2M$ vectors $|\delta_k\rangle\otimes|\pm\rangle$ with $\delta_k = 2\pi k/M$ ($k = 0, \pm1, \pm2, \ldots, \pm(M-1)/2$), and $|\pm\rangle$ the eigenvector of $\hat{\sigma}_3$. The Hamiltonian is thus represented as a $2M \times 2M$ matrix in this basis and diagonalized numerically. We choose the parameter M large enough to guarantee convergence of the eigenvalues.

Once the spectrum is known, we use the transition frequencies from the ground state, $\omega_n = E_n - E_{\rm GS}$, to do a least-square fit to the experimental data. The details of the numerical procedure are listed in the Jupyter notebooks available at [43].

Once an eigenstate $|\Psi\rangle$ is determined numerically, we represent its two-component wave function in the basis of the weak link eigenstates $\{|g\rangle, |e\rangle\}$ from Eq. (S10), evaluated at $\phi = \varphi$:

$$|\Psi\rangle = \sum_{\delta}\sum_{\sigma=g,e} \Psi(\delta,\sigma)|\delta,\sigma\rangle\,, \quad \Psi(\delta,\sigma) = \langle\delta,\sigma|\Psi\rangle\,, \tag{S13}$$

where

$$|\delta,\sigma\rangle = |\delta\rangle \otimes (c_{\sigma+}(\varphi)\,|+\rangle + c_{\sigma-}(\varphi)\,|-\rangle)\,. \tag{S14}$$

The probability densities $|\Psi(\delta,\sigma)|^2$ plotted in Fig. 4b and Fig. S6b allow us to evaluate at a glance whether the eigenstate $|\Psi\rangle$ has a large overlap with the excited state $\sigma = |e\rangle$ of the (decoupled) weak link.

Finally, in Fig. 3c we show the numerical prediction for the visibility of the ABS transition as a function of the phase bias, ϕ. The visibility is determined by the absolute square of current operator matrix element $\langle GS|\,\hat{J}(\varphi)\,|\Psi\rangle$ between the ground state $|GS\rangle$ and the excited state $|\Psi\rangle$ of $\hat{H}$ corresponding to the ABS transition. The current operator is [42]

$$\hat{J}(\varphi) = E_J\,\sin(\hat{\delta}) + \frac{\partial H_{\rm ABS}(\varphi - \hat{\delta})}{\partial\,\hat{\delta}}\,. \tag{S15}$$

Equilibrium phase drop

In the main text, we have often assumed that the equilibrium phase drop across the weak link, ϕ, is close to the total applied phase, $\phi \approx \varphi$. Here, we verify this assumption by calculating the equilibrium phase drop of the hybrid SQUID model we presented in the previous section.

Since $\phi = \varphi - \delta$, (see Eq. (S5)), it is sufficient to show that the equilibrium phase drop $\delta \equiv \langle GS|\hat{\delta}|GS\rangle$ across the tunnel junction is small. δ is given by the position where the ground state Josephson energy of Eq. (S5) is minimal for $E_C = 0$. From this condition, after taking a derivative of the Josephson energy, we obtain the following transcendental equation for δ:

$$E_J\sin(\delta) + \frac{\Delta\,T}{4}\,\frac{\sin(\delta - \varphi)}{\sqrt{1 - T\sin^2[(\varphi - \delta)/2]}} = 0\,. \tag{S16}$$

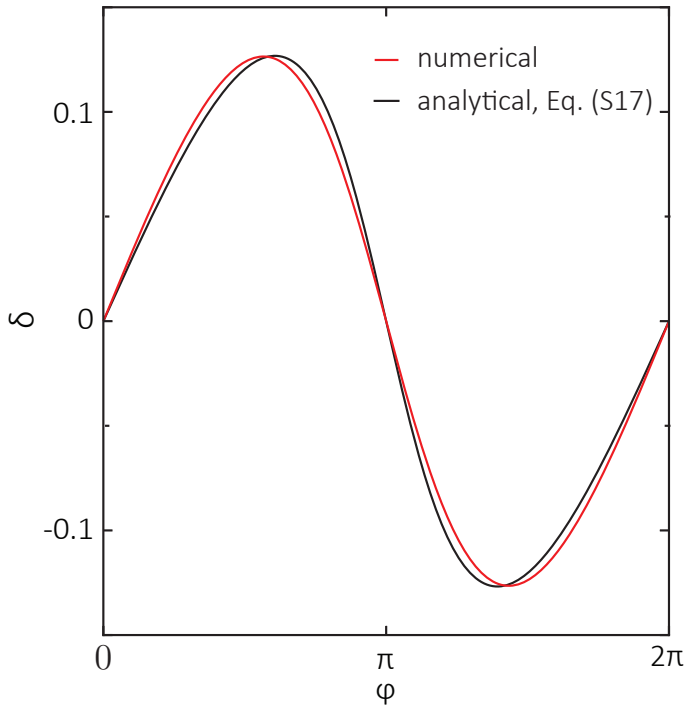

FIG. S8. **Equilibrium phase drop δ across the tunnel junction.** The black line is given by Eq. (S17), the red line by the numerical solution of Eq. (S16). In both cases, we use the same circuit parameters as in Fig. 3a of the main text: $\Delta = 122\,\mu$eV, $T = 0.57$, $E_C = 25.44\,\mu$eV, $E_J = 165\,\mu$eV.

For $E_J \gg \Delta T/4$, a good approximate solution is given by

$$\delta \approx \frac{\Delta\, T}{4E_J}\, \frac{\sin(\varphi)}{\sqrt{1 - T\sin^2(\varphi/2)}}\,. \tag{S17}$$

up to quadratic corrections in $(\Delta T/E_J)$. In Fig. S8 we show that for the parameters used in Fig. 3a, this approximate solution is very close to the exact, numerical one. Both exhibit a sinusoidal behavior with a maximum $\delta \approx 0.12$ at $\varphi \approx \pi/2$. This confirms that the phase drop across the weak link, $\phi = \varphi - \delta$, remains very close to the applied phase φ everywhere. In particular, ϕ is exactly equal to φ at $\varphi = n\pi$, where n is integer.

Andreev bound states in a proximitized Rashba nanowire in a parallel magnetic field

In this Section, we introduce the model used to describe the behavior of ABS as a function of the magnetic field B. We start from the standard Bogoliubov-de Gennes (BdG) Hamiltonian of a Rashba quantum wire with proximitized s-wave superconductivity and an external Zeeman field [44, 45]:

$$H_{\rm BdG} = -\left(\frac{\partial_x^2}{2m} - E_F\right)\tau_z - i\,\alpha\,\partial_x\, s_z\,\tau_z + E_Z\, s_x + \Delta\, e^{i\phi\,\theta(x)\,\tau_z}\,\tau_x + V\,\delta(x)\,\tau_z\,. \tag{S18}$$

Here, the two sets of Pauli matrices $\tau_{x,y,z}$ and $s_{x,y,z}$ act in the Nambu and spin spaces, respectively; $m = 0.023 m_{\rm e}$ is the effective mass in InAs [46], α is the Rashba spin-orbit coupling strength which defines $E_{\rm SO} = m\alpha^2/2$. $E_Z = \frac{1}{2}\, g\,\mu_B\, B$ is the Zeeman energy, Δ is the proximity induced gap and θ is the Heaviside step function. The Fermi level E_F is measured from the middle of the Zeeman gap in the normal state band dispersion, see Fig. S9. Note that starting with Eq. (S18) we set $\hbar = 1$. The superconducting phase difference between the left lead ($x < 0$) and the right lead ($x > 0$) is denoted by ϕ. The last term of Eq. (S18) models a short-range scatterer at $x = 0$, accounting for the finite channel transmission.

We seek bound state solutions of the the BdG equations,

$$H_{\rm BdG}\,\Psi(x) = E\,\Psi(x)\,, \tag{S19}$$

at energies $|E| < \Delta$. We will consider in particular two opposite regimes: (a) $E_F \gg E_{\rm SO}, E_Z, \Delta$ and (b) $E_F = 0$, see the two insets in the corresponding panels of Fig. S9. In order to find bound state solutions we proceed as follows:

1. We linearize the BdG equations for the homogeneous system ($V = 0, \phi = 0$) around $E = E_F$. In this way, we obtain two effective low-energy Hamiltonians, $H^{(a)}_{\rm eff}$ and $H^{(b)}_{\rm eff}$, which are linear in the spatial derivative. They can be written as:

$$H^{(a)}_{\rm eff} = -iv\,\partial_x\,\tau_z\,\sigma_z - vq_0\,\tau_z\,\rho_z + \frac{\Delta\,\alpha\,k_F}{vq_0}\,\tau_x\sigma_z + \frac{\Delta\,E_Z}{vq_0}\,\tau_y\,\rho_y\,, \tag{S20a}$$

$$H^{(b)}_{\rm eff} = -i\alpha\,\partial_x\,\tau_z\,\sigma_z + \Delta\tau_x + \tfrac{1}{2}\,E_Z\,\sigma_z\,(1-\rho_z)\,. \tag{S20b}$$

   We now have three sets of Pauli matrices: $\tau_{x,y,z}$ (Nambu space), $\rho_{x,y,z}$ (distinguishing the inner/outer propagating modes, and replacing the spin matrices $s_{x,y,z}$ of Eq. (S18)), and $\sigma_{x,y,z}$ (distinguishing left- and right-moving modes, and not to be confused with the σ matrices used in the previous Section). For regime (a), we have also introduced the Fermi momentum $k_F = \sqrt{2mE_F}$, the Fermi velocity $v = k_F/m$ and the energy difference $vq_0 = \sqrt{\alpha^2 k_F^2 + E_Z^2}$ between the two helical bands at the Fermi momentum. Note that, in the regime (b) where $E_F = 0$, the linearization requires $E_{\rm SO} \gg \Delta, E_Z$, so it corresponds to the limit of strong spin-orbit coupling.

2. Using Eq. (S18), we compute the transfer matrix $\mathcal{T}$ of the junction in the normal state ($\Delta = 0$), at energy $E = E_F$. The transfer matrix gives a linear relation between the plane-wave coefficients of the general solution on the left and right hand sides of the weak link. In computing $\mathcal{T}$, we neglect all terms $\propto E_F^{-1}$ in regime (a). In regime (b), the transfer matrix is computed for $E_Z = 0$, since the effect of magnetic field on scattering can be neglected to due the small dwelling time in the short junction. At $E_Z = 0$, the transfer matrix depends on the single real parameter T, the transmission probability of the junction. The latter is given by $T = 4k_F^2/(4k_F^2 + V^2)$ in regime (a), and $T = 1/(1 + V^2/\alpha^2)$ in regime (b).

3. Using the transfer matrix $\mathcal{T}$ as the boundary condition at $x = 0$ for the linearized BdG equations, we obtain the following bound state equation for E:

$$\det\,\left[1 - G(E)\,\tau_z\,\sigma_z\,\left(e^{-i\phi\,\tau_z/2}\,\mathcal{T} - 1\right)\right] = 0\,, \tag{S21}$$

   where $G(E)$ is the integrated Green's function,

$$G(E) = v\int\frac{{\rm d}q}{2\pi i}\,e^{-iq\cdot 0}\,[H_{\rm eff}(q) - E]^{-1}\,, \tag{S22}$$

   and $H_{\rm eff}(q)$ is the Fourier transform of either of the linearized Hamiltonians of Eq. (S20a). [In regime (b), v must be replaced by α in the expression for $G(E)$]. In deriving the bound state equation, we have neglected the energy dependence of the transfer matrix, which is appropriate in the short junction limit. In regime (b), this also requires that the length of the junction is shorter than α/E_Z, so that we can neglect resonant effects associated with normal-state quasi-bound states in the Zeeman gap, which would lead to a strong energy dependence of the transmission [47]. Eq. (S21) is analogous to the bound state equation for the ABS derived in Ref. [48], except that it is formulated in terms of the transfer matrix of the weak link, rather than its scattering matrix. Unlike its counterpart, Eq. (S21) incorporates the effect of the magnetic field in the superconducting leads. It is thus appropriate to study the effect of a magnetic field on the ABS in the limit of uniform penetration of the field in the superconductor.

After performing the integral for $G(E)$, the roots of Eq. (S21) can be determined numerically. For the two regimes, this leads to the typical behavior of the ABS shown in Fig. S9 against the experimental data. We find a better agreement with the experimental data for regime (a), as discussed in the main text.

A more detailed theoretical study of Eq. (S21), including a detailed analysis of its roots at finite magnetic fields and the code used in the numerical solution, is in preparation. It will also be interesting to extend the current model beyond the linearization to allow the calculation of the spectrum at arbitrary values of E_F.

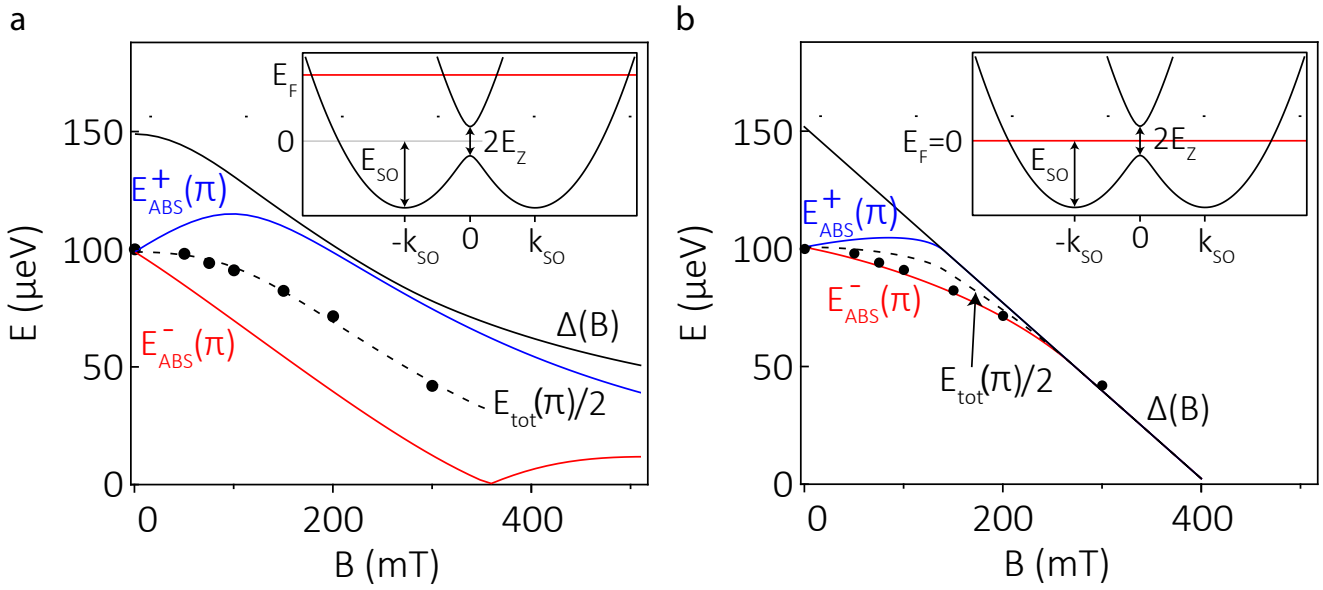

FIG. S9. **Comparison between the magnetic-field dependence of ABS spectra in the low and high Fermi level regimes.** The left panel reproduces the best-fit theoretical spectrum for regime (a) - the same shown in Fig. 4b of the main text - with free parameters $g = 12 \pm 1$ and $\sqrt{E_{\rm SO} E_F}/\Delta = 0.22 \pm 0.01$. The right panel shows the best-fit theoretical spectrum for regime (b), determined by a single free parameter $g = 12.9 \pm 0.3$. Note that: (i) the spectrum on the right hand side does not predict a fermion-parity switch preceding the gap closing at $E_Z \approx 400$ mT; (ii) at $B = 300$ mT, the last data point falls in the continuum part of the energy spectrum, in contradiction with the flux dispersion of the corresponding spectral line observed in experimental data. For these reasons, we believe that the experimental data is better described by the high Fermi level regime, as presented in the main text. We however cannot exclude the possibility that an intermediate value $0 \lesssim E_F \lesssim E_{\rm SO}$ may also provide a good fit.

[39] F. Kos, S. E. Nigg, and L. I. Glazman, Phys. Rev. B **87**, 174521 (2013).
[40] L. Bretheau, Ç. Girit, M. Houzet, H. Pothier, D. Esteve, and C. Urbina, Phys. Rev. B **90**, 134506 (2014).
[41] A. Zazunov, V. S. Shumeiko, E. N. Bratus, J. Lantz, and G. Wendin, Phys. Rev. Lett. **90**, 087003 (2003).
[42] A. Zazunov, V. S. Shumeiko, G. Wendin, and E. N. Bratus, Phys. Rev. B **71**, 214505 (2005).
[43] Http://dx.doi.org/10.4121/uuid:bfcc43f5-4077-4f1c-84d6-95feb6f3d8e6.
[44] R. M. Lutchyn, J. D. Sau, and S. Das Sarma, Phys. Rev. Lett. **105**, 077001 (2010).
[45] Y. Oreg, G. Refael, and F. von Oppen, Phys. Rev. Lett. **105**, 177002 (2010).
[46] I. Vurgaftman, J. R. Meyer, and L. R. Ram-Mohan, Journal of Applied Physics **89**, 5815 (2001).
[47] K. N. Nesterov, M. Houzet, and J. S. Meyer, Phys. Rev. B **93**, 174502 (2016).
[48] C. W. J. Beenakker, Phys. Rev. Lett. **67**, 3836 (1991)